Metallic Conduction and Ferromagnetism in MAl2O4/SrTiO3 Spinel/Perovskite Heterostructures (M=Fe, Co, Ni)

Zhang, Yu ; Gan, Yulin; Zhang, Hongrui ; Zhang, Hui ; Norby, Poul; Shen, Baogen; Sun, Jirong; Chen, Yunzhong

Published in:
Applied Physics Letters

Link to article, DOI:
10.1063/1.5063540

Publication date:
2018

Document Version
Peer reviewed version

Metallic Conduction and Ferromagnetism in $MAl_2O_4/SrTiO_3$ Spinel/Perovskite Heterostructures (M = Fe, Co, Ni)

Yu Zhang,[1,3] Yulin Gan,[2] Hongrui Zhang,[1,3] Hui Zhang, [1,3] Poul Norby,[2] Baogen Shen,[1,3] Jirong Sun,[1,3, a)] and Yunzhong Chen[2, a)]

[1]Beijing National Laboratory for Condensed Matter Physics and Institute of Physics, Chinese Academy of Sciences, Beijing 100190, Peoples' Republic of China

[2]Department of Energy Conversion and Storage, Technical University of Denmark, Risø Campus, 4000 Roskilde, Denmark

[3]School of Physical Sciences, University of Chinese Academy of Sciences, Beijing 100049, Peoples' Republic of China

Electronic mail: jrsun@iphy.ac.cn; yunc@dtu.dk

Abstract:

Recently, a high mobility quasi-two-dimensional electron gas (q-2DEG) has been reported for the heterointerface between two insulating and nonmagnetic oxides of spinel γ-Al_2O_3 and perovskite $SrTiO_3$ (STO). Herein, we fabricated the epitaxial heterostructure with Al-based magnetic spinel oxide MAl_2O_4 (M = Fe, Co, Ni) on perovskite STO. Remarkably, all the MAl_2O_4 (M = Fe, Co, Ni) films exhibit ferromagnetic behavior up to room temperature. Although the $FeAl_2O_4$/STO is insulating, the $NiAl_2O_4$/STO and $CoAl_2O_4$/STO heterointerfaces are found to be highly metallic and exhibit anomalous Hall effect (AHE) at temperatures below 30 K. Their Hall mobility is as high as 3×10^4 $cm^2V^{-1}s^{-1}$, comparable to that of γ-Al_2O_3/STO interface. There has been evidence of oxygen-vacancy-related magnetism in γ-Al_2O_3/STO at temperatures below 5 K, while the enhanced AHE in $NiAl_2O_4$/STO and $CoAl_2O_4$/STO likely comes from the magnetic proximity effect induced by the top ferromagnetic MAl_2O_4 spinel films.

The metallic interface between two insulating oxides, where a quasi-two-dimensional electron gas (q-2DEG) resides, provides a promising platform for the exploration of emergent phenomena.[1,2] Its attractive physical properties, such as superconductivity,[3] ferromagnetism,[4] high electron mobility,[5] strong gating field,[6,7] quantum Hall effect,[8] and photo excitation effect,[9,10] have drawn extensive interest. So far, the isostructural perovskite-type interface, particularly $LaAlO_3/SrTiO_3$ (LAO/STO)[1] has been investigated intensively. However, the high mobility q-2DEG discovered at the non-isostructural interface between spinel γ-Al_2O_3 and perovskite STO remains underinvestigated.[2,11–14] In addition to the remarkably high electron mobility (1.4×10^5 $cm^2V^{-1}s^{-1}$ at 2 K), the spinel structure of γ-Al_2O_3 also provides the opportunity to introduce intrinsic ferromagnetism into the heterostructure, which remains unexplored.

Herein, we epitaxially grew three new heterostructures, consisting of $M$$Al_2O_4$ (M = Fe, Co, Ni) top films and (001)-oriented TiO_2-terminated STO substrates, and investigated their interfacial conduction and ferromagnetism. Remarkably, all the $M$$Al_2O_4$ (M = Fe, Co, Ni) films exhibit ferromagnetic behavior up to room temperature. We further found that the $NiAl_2O_4$/STO and $CoAl_2O_4$/STO interfaces are metallic and ferromagnetic at low temperatures, as indicated by the appearance of anomalous Hall effect (AHE). The AHE of the $M$$Al_2O_4$/STO interfaces ($M$ = Ni, Co) remains sizable up to 30 K, in contrast to γ-Al_2O_3/STO which shows AHE below 5 K. Moreover, the anomalous Hall resistance (R_{AHE}) undergoes a negative to positive sign change when the top film of the heterostructure changes from γ-Al_2O_3 to $M$$Al_2O_4$. We proposed that the AHE in γ-Al_2O_3/STO is due to the oxygen vacancies induced ferromagnetism in proximity to the STO surface, while the AHE in $NiAl_2O_4$/STO and $CoAl_2O_4$/STO probably comes from the magnetic proximity effect induced by the ferromagnetic $M$$Al_2O_4$ spinel films. Different from $NiAl_2O_4$/STO and $CoAl_2O_4$/STO interfaces, $FeAl_2O_4$/STO is insulating.

Films were grown on TiO_2-terminated STO single crystal substrates (5 mm × 5 mm × 0.5 mm in dimensions) by pulsed laser deposition using a KrF laser with a wavelength of 248 nm. During deposition, the substrate temperature was maintained at 650 ºC and the oxygen pressure was kept at 1×10^{-5} mbar. The laser fluence was 2 Jcm^{-2} and the repetition rate was 1 Hz. The target-substrate distance was fixed at 5 cm. After deposition, the samples were cooled to room temperature without changing oxygen pressure. For the γ-Al_2O_3 deposition, a commercial Al_2O_3 single crystal target was used. MAl_2O_4 (*M* = Fe, Co, Ni) ceramic targets were adopted for other films. These targets were prepared by sintering the mixture of appropriate amounts of Al_2O_3 with Fe_2O_3, Co_3O_4 and NiO powders first, at 1200 ºC for 10 h and then, after pressing, at 1350 ºC for 36 h. The film growth rate is approximate 0.08 Å/s. The epitaxial growth of the crystalline films was confirmed by both reflection high-energy electron diffraction (RHEED) and high-resolution X-ray diffraction (XRD) measurements. Heterostructures with 4 nm thickness top films are employed for transport and magnetic measurements. While, heterostructures with 40 nm top films are used for XRD measurements. Ultrasonic Al wire bonding was used to get electric connection, and the van der Pauw geometry was adopted.

Fig. 1(a) is a schematic illustration of the spinel/perovskite (MAl_2O_4/STO) oxide heterostructure. The epitaxial growth of spinel MAl_2O_4 (*M* = Fe, Co, Ni) films on perovskite STO substrate is due to their compatible oxygen sub-lattice, as the lattice parameter of MAl_2O_4 is about twice that of STO.[2] Although γ-Al_2O_3 and STO show a good lattice match (1%), $NiAl_2O_4$, $CoAl_2O_4$, and $FeAl_2O_4$ exhibit larger lattice mismatch with STO substrate (> 3%) as summarized in Table I. Consequently, the γ-Al_2O_3 film can been epitaxially grown on STO (001) substrate with a persistent layer-by-layer two-dimensional growth mode as confirmed by RHEED and high-resolution transmission electron microscopy,[13,15] while the $NiAl_2O_4$, $CoAl_2O_4$, and $FeAl_2O_4$ films show 3D island growth mode. Despite of this, the epitaxial growth of $NiAl_2O_4$, $CoAl_2O_4$, and $FeAl_2O_4$ films

with the thickness of 40 nm on STO is confirmed by the XRD measurements. As shown in Figs. 1(b), for the θ - 2θ scan in the region of 10º - 80º, (004) spinel Bragg peaks is observed on the left side of the corresponding STO peaks of (002). The out-of-line lattice parameters of γ-Al_2O_3, $NiAl_2O_4$, $CoAl_2O_4$, and $FeAl_2O_4$ films determined by XRD are 8.02, 8.03, 8.08, and 8.16 Å, respectively. This indicates that all the $M$$Al_2O_4$ films are well strain-relaxed. In addition, for the films of $NiAl_2O_4$ and $FeAl_2O_4$, impurity phase of $M$$AlO_2$ (M = Ni, Fe) at 16.6º is detected. For $NiAl_2O_4$ film, an extra impurity phase of Ni (200) crystal phase at 51.7º is also observed. These impurity phases could stem from the reduction environment of low oxygen pressure (1×10^{-5} mbar) and high temperature (650 ºC) adopted during the film deposition.[16] However, the low diffraction intensity indicates that the amount of these impurities is rather low. Notably, these impurity phases survive after the post annealing at 300°C in 1 bar oxygen for 3 hours, meanwhile, the interface becomes insulating. Therefore, such impurity phases contribute negligibly to the interface conduction as discussed later. This is also consistent with the fact that $M$$Al_2O_4$ (M = Fe, Co, Ni) films grown on $(LaAlO_3)_{0.3}(Sr_2TaAlO_6)_{0.7}$ (LSAT) substrates are insulating in nature (see in Supplemental Material S1). Fig. 1(c) shows the Rocking curves of the (004) spinel films grown on STO substrates. The full widths at half maximum (FWHM) of the curves determined by Gaussian fitting are shown in Table I. All $M$$Al_2O_4$ (M = Fe, Co, Ni) films display good crystallinity. In addition, comparing to $M$$Al_2O_4$ spinel films, the relatively larger FWHM (0.21º) of γ-Al_2O_3 film might be due to its less ordered crystallographic structure which contains cation vacancies.[17]

Transport measurements show that $FeAl_2O_4$/STO is highly insulating. However, the metallic conduction is obtained in γ-Al_2O_3/STO, $M$$Al_2O_4$/STO ($M$ = Ni, Co) heterostructures, as shown in Fig. 2(a). Comparing to γ-Al_2O_3/STO whose sheet resistance (R_s) is 278 Ω/□ at room temperature, the $NiAl_2O_4$/STO and $CoAl_2O_4$/STO have smaller R_s which are 57.8 Ω/□ and 138 Ω/□, respectively. Figs. 2(b)-(d) display the Hall resistance (R_{xy}) of γ-Al_2O_3/STO, $NiAl_2O_4$/STO and $CoAl_2O_4$/STO as

a function of magnetic field (B) in the temperature range from 295 to 2 K. When temperature is high (T > 100 K), R_{xy} varies linearly with applied field for all samples. This is the typical behavior of the normal Hall effect (NHE). Cooling the samples to 100 K, R_{xy} shows nonlinear dependence on magnetic field. In the meanwhile, the magnetic field-dependent magnetoresistance (MR = ($R_{xx}(B)/Rxx(B=0)$-1) traces follow a bell-like shape, where MR-B displays a U-shape at low field, and shift to a bell-shape at high field. These features suggest that the conductivity comes from two or more carriers as previously reported by Joshua *et al.*[18] and Kim *et al.*[19], and can be fitted by a two-band model (see Supplemental Material S2). However, the R_{xy} exhibits a stronger curvature in the low-field range when further cooled below a critical temperature of approximately 30 K, which is beyond the capture of the two-band model. To describe the R_{xy}-B relation at T<30 K, we adopted an extended two-band model that combines the two-band conduction-dominated NHE with an AHE as reported before[20,21] (see Supplemental Material S2):

$$R_{xy} = R_{NHE} + R_{AHE} = R_{NHE} + \alpha L(\frac{mB}{k_B T}) \quad (1)$$

where R_{NHE} and R_{AHE} represent the Hall resistance from two-band conduction and AHE, respectively. The Langevin function L is introduced to simulate the step-shaped AHE curve in form, α is a scale factor, and m is magnetic moment.

Fig. 2(e) displays the determination of the anomalous Hall resistance, R_{AHE}, from R_{xy}. The results of *eq.* 1 (thin black line) well reproduce the measured R_{xy} (thick green line). Basically, the normal Hall resistance (R_{NHE}) varies smoothly with B in the whole field range, with slightly but identifiable curve bending. In contrast, R_{AHE} is constant in high-field range and undergoes a drastic change as B sweeps through zero field. It also becomes clear that AHE appears below 5 K for γ-Al_2O_3/STO, and 30 K for both $NiAl_2O_4$/STO and $CoAl_2O_4$/STO. Based on the R_{NHE} in *eq.* 1, the temperature-dependent density (n_s) and Hall mobility (μ) of the carriers confined in heterostructures

can be deduced (Figs. 2(f)-(g)). The n_s of q-2DEGs is nearly constant from 295 K to 2 K. At 2 K, the γ-Al_2O_3/STO possesses the lowest n_s with a value of 3×10^{15} cm^{-2}. The $NiAl_2O_4$/STO heterointerface has the highest n_s (2.2×10^{16} cm^{-2}) which is higher than γ-Al_2O_3/STO by a factor of 7. The n_s of $CoAl_2O_4$/STO is 9.8×10^{15} cm^{-2}. These extremely high carrier densities indicate that 3D STO bulk conduction contributes to the measured conductivity. With regards to the μ, these three heterostructures have comparable values in the range of 2.7 - 3.4×10^4 $cm^2V^{-1}s^{-1}$ at 2 K, also consistent with the mobility for bulk STO.[1,13] It is noteworthy that the $FeAl_2O_4$/STO grown under the same condition with $NiAl_2O_4$/STO and $CoAl_2O_4$/STO is highly insulating. This means that the Al-based spinel/perovskite interface is extremely sensitive to the introduction of the magnetic ions.

The metallic conduction in STO-based heterostructures comes from electrons located on the STO side. The high n_s in γ-Al_2O_3/STO and $M$$Al_2O_4$/STO ($M$ = Ni, Co) could result from the formation of oxygen vacancies in STO due to interfacial redox reactions.[2,13,15,22] However, the insulating $FeAl_2O_4$/STO heterointerface might stem from two reasons. On the one hand, the Fe-based oxide has poor ability to reduce STO substrate during the film deposition.[23] On the other hand, the band gap of $FeAl_2O_4$ (1.78 eV[24]) is much lower than that of STO (3.2 eV), any reconstructed electrons tend to accumulate in the spinel films rather than transferring to the heterointerface.[25]

Figs. 3(a)-(c) show the R_{AHE} variation with respect to B at different temperatures for γ-Al_2O_3/STO, $M$$Al_2O_4$/STO ($M$ = Ni, Co). The R_{AHE} of γ-Al_2O_3/STO has the same sign to B, while that of $M$$Al_2O_4$/STO ($M$ = Ni, Co) are opposite to B. Similar crossover in the sign of R_{AHE} has also been observed between $SrRuO_3$ and $La_{1-x}Sr_xCoO_3$ (x=0.17) crystals.[26] But the explanation for such phenomenon remains open, which could result from the intrinsic different origins of the magnetism. Moreover, in the magnetic saturation state, such as under B = -10 T at 2 K, R_{AHE} is as large as 0.013 Ω for γ-Al_2O_3/STO, while it is 0.008 Ω for $NiAl_2O_4$/STO and 0.012 Ω for $CoAl_2O_4$/STO. Fig. 3(d)

summarizes the R_{AHE} for these three heterointerfaces as a function of temperature. Clearly, the AHE appears at $T \leq 30$ K for MAl$_2$O$_4$/STO (M = Ni, Co), whereas, only below 5 K for γ-Al$_2$O$_3$/STO as discussed before. Shortly, the AHE of the MAl$_2$O$_4$/STO (M = Ni, Co) is dramatically different from that of γ-Al$_2$O$_3$/STO.

In order to uncover the origin of AHE in γ-Al$_2$O$_3$/STO and MAl$_2$O$_4$/STO (M = Ni, Co) heterointerfaces, magnetic measurements were performed by superconducting quantum interference device (SQUID) magnetometer (as shown in Fig. 3(e)). Remarkably, these three MAl$_2$O$_4$/STO (M = Fe, Co, Ni) heterostructures exhibit unexpected ferromagnetic properties up to room temperature. Notably, the CoAl$_2$O$_4$ and FeAl$_2$O$_4$ show spin-glass-like ground states in bulk below the Curie-Weiss temperatures (5 K for CoAl$_2$O$_4$ and 12 K for FeAl$_2$O$_4$),[27,28] and the NiAl$_2$O$_4$ is paramagnetic.[29] In the meantime, the ferromagnetism of γ-Al$_2$O$_3$/STO is very weak (see Supplementary Material S3). At room temperature (inset of Fig. 3(e)), the magnetizations of FeAl$_2$O$_4$, CoAl$_2$O$_4$ and NiAl$_2$O$_4$ are 135.3, 76.4 and 69.4 emu/cm^3 when B = 6 T, respectively, which are much lower than the magnetization of Fe$_3$O$_4$ (about 480 emu/cm^3 at room temperature).[30] When the temperature is 10 K, FeAl$_2$O$_4$ has the strongest magnetization, which is as large as 291.3 emu/cm^3 at B = 6 T, while CoAl$_2$O$_4$ and NiAl$_2$O$_4$ have comparable magnetization, which are 196.2 and 177.9 emu/cm^3, respectively. As for the interface between γ-Al$_2$O$_3$ and STO, the conduction comes from the oxygen vacancies, which could result in ferromagnetism, thus, the AHE as the origin of the ferromagnetism in LAO/STO.[31–33] These oxygen vacancies not only induce a complex multi-orbital reconstruction thus the mobile q-2DEG, but also result the spin splitting of the electronic states, giving rise to localized Ti 3d electrons thus magnetism. Salluzzo *et al.* [33] experimentally proved that the oxygen vacancies play a decisive role in the interfacial magnetism in LAO/STO. Whereas, the much higher upper limit temperature (30 K) of AHE observed in our

MAl$_2$O$_4$/STO (M = Ni, Co) heterostructures than that of γ-Al$_2$O$_3$/STO (5 K) indicates that the oxygen-vacancy-related AHE in MAl$_2$O$_4$/STO is relatively weak.

It has also been suggested that interdiffusion of magnetic cations into STO could result in a similar transport behavior in manganite-buffered LAO/STO heterostructure.[20] Since the interdiffusion of cations is also a common phenomenon in the spinel/perovskite heterostructure, such as γ-Al$_2$O$_3$/STO.[2] Therefore, we cannot rule out the possibility of the interdiffusion of magnetic ions into STO as a possible origin of AHE at MAl$_2$O$_4$/STO heterointerfaces. However, such interdiffusion of magnetic ions into STO could result in Kondo effect, which is absent here. Finally, since the top films are found to be ferromagnetic, we therefore assume that the AHE in MAl$_2$O$_4$/STO (M = Ni, Co) comes from the magnetism induced by a magnetic proximity effect as reported for the EuTiO$_3$-buffered LAO/STO heterostructure.[34]

In summary, we epitaxially grown MAl$_2$O$_4$/STO (M = Fe, Co, Ni) heterostructures in comparison to the γ-Al$_2$O$_3$/STO heterostructure. Remarkably, all the MAl$_2$O$_4$ (M = Fe, Co, Ni) films exhibit ferromagnetic behavior up to room temperature. The heterointerface of FeAl$_2$O$_4$/STO is highly insulating. In contrast, the NiAl$_2$O$_4$/STO and CoAl$_2$O$_4$/STO are metallic conducting. AHE is observed in most of the metallic interfaces of γ-Al$_2$O$_3$/STO, NiAl$_2$O$_4$/STO and CoAl$_2$O$_4$/STO. While the AHE in γ-Al$_2$O$_3$/STO is likely due to the magnetism induced by oxygen vacancies, the AHE in NiAl$_2$O$_4$/STO and CoAl$_2$O$_4$/STO most likely comes from the magnetic proximity effect induced by the top ferromagnetic spinel films.

Supplementary Material

See supplementary material for XRD data of NiAl$_2$O$_4$ films prepared under different oxygen pressures, on different substrates (STO, LSAT) and after the post oxygen annealing; Two-band model fitting of interface conduction; Magnetization of spinel/perovskite heterostructures.

Acknowledgements:

We acknowledge the support of the National Basic Research of China (No. 2016YFA0300701), the National Natural Science Foundation of China (Nos. 11520101002 and 51590880), and the Key Program of the Chinese Academy of Sciences.

References:

[1] A. Ohtomo and H.Y. Hwang, Nature **427**, 423 (2004).

[2] Y.Z. Chen, N. Bovet, F. Trier, D. V. Christensen, F.M. Qu, N.H. Andersen, T. Kasama, W. Zhang, R. Giraud, J. Dufouleur, T.S. Jespersen, J.R. Sun, A. Smith, J. Nygård, L. Lu, B. Büchner, B.G. Shen, S. Linderoth, and N. Pryds, Nat. Commun. **4**, 1371 (2013).

[3] N. Reyren, S. Thiel, A.D. Caviglia, L. Fitting Kourkoutis, G. Hammerl, C. Richter, C.W. Schneider, T. Kopp, A.-S. Rüetschi, D. Jaccard, M. Gabay, D.A. Muller, J.-M. Triscone, and J. Mannhart, Science **317**, 1196 (2007).

[4] A. Brinkman, M. Huijben, M. Van Zalk, J. Huijben, U. Zeitler, J.C. Maan, W.G. Van Der Wiel, G. Rijnders, D.H.A. Blank, and H. Hilgenkamp, Nat. Mater. **6**, 493 (2007).

[5] Y.Z. Chen, F. Trier, T. Wijnands, R.J. Green, N. Gauquelin, R. Egoavil, D. V. Christensen, G. Koster, M. Huijben, N. Bovet, S. Macke, F. He, R. Sutarto, N.H. Andersen, J.A. Sulpizio, M. Honig, G.E.D.K. Prawiroatmodjo, T.S. Jespersen, S. Linderoth, S. Ilani, J. Verbeeck, G. Van Tendeloo, G. Rijnders, G.A. Sawatzky, and N. Pryds, Nat. Mater. **14**, 801 (2015).

[6] W. Niu, Y. Zhang, Y. Gan, D. V. Christensen, M. V. Soosten, E.J. Garcia-Suarez, A. Riisager, X. Wang, Y. Xu, R. Zhang, N. Pryds, and Y. Chen, Nano Lett. **17**, 6878 (2017).

[7] W.N. Lin, J.F. Ding, S.X. Wu, Y.F. Li, J. Lourembam, S. Shannigrahi, S.J. Wang, and T. Wu, Adv. Mater. Interfaces **1**, 1300001 (2014).

[8] F. Trier, G.E.D.K. Prawiroatmodjo, Z. Zhong, D.V. Christensen, M. Von Soosten, A. Bhowmik, J.M.G. Lastra, Y. Chen, T.S. Jespersen, and N. Pryds, Phys. Rev. Lett. **117**, 096804 (2016).

[9] Y. Lei, Y. Li, Y.Z. Chen, Y.W. Xie, Y.S. Chen, S.H. Wang, J. Wang, B.G. Shen, N. Pryds, H.Y. Hwang, and J.R. Sun, Nat. Commun. **5**, 5554 (2014).

[10] H. Yan, Z. Zhang, S. Wang, H. Zhang, C. Chen, and K. Jin, ACS Appl. Mater. Interfaces **9**, 39011 (2017).

[11] D. V. Christensen, M. von Soosten, F. Trier, T.S. Jespersen, A. Smith, Y. Chen, and N. Pryds, Adv. Electron. Mater. **3**, 1700026 (2017).

[12] P. Schütz, F. Pfaff, P. Scheiderer, Y.Z. Chen, N. Pryds, M. Gorgoi, M. Sing, and R. Claessen, Phys. Rev. B **91**, 165118 (2015).

[13] Y.Z. Chen, N. Bovet, T. Kasama, W.W. Gao, S. Yazdi, C. Ma, N. Pryds, and S. Linderoth, Adv. Mater. **26**, 1462 (2014).

[14] S.W. Lee, Y. Liu, J. Heo, and R.G. Gordon, Nano Lett. **12**, 4775 (2012).

[15] T.Q. Ngo, N.J. Goble, A. Posadas, K.J. Kormondy, S. Lu, M.D. McDaniel, J. Jordan-Sweet, D.J. Smith, X.P.A. Gao, A.A. Demkov, and J.G. Ekerdt, J. Appl. Phys. **118**, 115303 (2015).

[16] Y.S. Jung, W.L. Yoon, Y.S. Seo, and Y.W. Rhee, Catal. Commun. **26**, 103 (2012).

[17] B. Ealet, M.H. Elyakhloufi, E. Gillet, and M. Ricci, Thin Solid Films **250**, 92 (1994).

[18] A. Joshua, S. Pecker, J. Ruhman, E. Altman, and S. Ilani, Nat. Commun. **3**, 1129 (2012).

[19] J.S. Kim, S.S.A. Seo, M.F. Chisholm, R.K. Kremer, H.U. Habermeier, B. Keimer, and H.N. Lee, Phys. Rev. B **82**, 201407 (2010).

[20] H.R. Zhang, Y. Zhang, H. Zhang, J. Zhang, X. Shen, X.X. Guan, Y.Z. Chen, R.C. Yu, N. Pryds, Y.S. Chen, B.G. Shen, and J.R. Sun, Phys. Rev. B **96**, 195167 (2017).

[21] F. Gunkel, C. Bell, H. Inoue, B. Kim, A.G. Swartz, T.A. Merz, Y. Hikita, S. Harashima, H.K. Sato, M. Minohara, S. Hoffmann-Eifert, R. Dittmann, and H.Y. Hwang, Phys. Rev. X **6**, 031035 (2016).

[22] K.J. Kormondy, A.B. Posadas, T.Q. Ngo, S. Lu, N. Goble, J. Jordan-Sweet, X.P.A. Gao, D.J. Smith, M.R. McCartney, J.G. Ekerdt, and A.A. Demkov, J. Appl. Phys. **117**, 095303 (2015).

[23] A.B. Posadas, K.J. Kormondy, W. Guo, P. Ponath, J. Geler-Kremer, T. Hadamek, and A.A. Demkov, J. Appl. Phys. **121**, 105302 (2017).

[24] H.Y. Mu, F.T. Li, X.T. An, R.H. Liu, Y.L. Li, X. Qian, and Y.Q. Hu, Phys. Chem. Chem. Phys. **19**, 9392 (2017).

[25] W. Niu, W. Liu, M. Gu, Y. Chen, X. Zhang, M. Zhang, Y. Chen, J. Wang, J. Du, F. Song, X. Pan, N. Pryds, X. Wang, P. Wang, Y. Xu, Y. Chen, and R. Zhang, Adv. Electron. Mater. **4**, 1800055 (2018).

[26] T. Miyasato, N. Abe, T. Fujii, A. Asamitsu, S. Onoda, Y. Onose, N. Nagaosa, and Y. Tokura, Phys. Rev. Lett. **99**, 086602 (2007).

[27] G.M. Kalvius, A. Krimmel, O. Hartmann, F.J. Litterst, R. Wäppling, V. Tsurkan, and A. Loidl, Phys. B Condens. Matter **404**, 660 (2009).

[28] N. Tristan, J. Hemberger, A. Krimmel, H.A. Krug Von Nidda, V. Tsurkan, and A. Loidl, Phys. Rev. B **72**, 174404 (2005).

[29] S. Kamali, J. Magn. Magn. Mater. **433**, 155 (2017).

[30] Y.Z. Chen, J.R. Sun, Y.N. Han, X.Y. Xie, J. Shen, C.B. Rong, S.L. He, and B.G. Shen, J. Appl. Phys. **103**, 07D703 (2008).

[31] N. Pavlenko, T. Kopp, E.Y. Tsymbal, G.A. Sawatzky, and J. Mannhart, Phys. Rev. B **85**, 020407 (2012).

[32] N. Pavlenko, T. Kopp, E.Y. Tsymbal, J. Mannhart, and G.A. Sawatzky, Phys. Rev. B **86**, 064431 (2012).

[33] M. Salluzzo, S. Gariglio, D. Stornaiuolo, V. Sessi, S. Rusponi, C. Piamonteze, G.M. De Luca, M. Minola, D. Marré, A. Gadaleta, H. Brune, F. Nolting, N.B. Brookes, and G. Ghiringhelli, Phys. Rev. Lett. **111**, 087204 (2013).

[34] D. Stornaiuolo, C. Cantoni, G.M. De Luca, R. Di Capua, E. Di Gennaro, G. Ghiringhelli, B. Jouault, D. Marrè, D. Massarotti, F.M. Granozio, I. Pallecchi, C. Piamonteze, S. Rusponi, F. Tafuri, and M. Salluzzo, Nat. Mater. **15**, 278 (2016).

[35] R.S. Zhou and R.L. Snyder, Acta Crystallogr. Sect. B **47**, 617 (1991).

[36] Y.S. Han, J.B. Li, X.S. Ning, and B. Chi, J. Am. Ceram. Soc. **87**, 1347 (2004).

[37] M.G. Brik, A. Suchocki, and A. Kamińska, Inorg. Chem. **53**, 5088 (2014).

[38] A. Walsh, S.H. Wei, Y. Yan, M.M. Al-Jassim, J.A. Turner, M. Woodhouse, and B.A. Parkinson, Phys. Rev. B **76**, 165119 (2007).

[39] M. Yazdanmehr, S.J. Asadabadi, A. Nourmohammadi, M. Ghasemzadeh, and M. Rezvanian, Nanoscale Res. Lett. **7**, 448 (2012).

[40] M.E. Gouda and W.A.A. Bayoumy, Int. J. Sci. Eng. Res. **6**, 328 (2015).

Table I. Lattice parameters of γ-Al_2O_3, MAl_2O_4 (M = Fe, Co, Ni) in bulk from reports and in film shown in text deduced by XRD data, their mismatches with STO substrate, the full widths at half maximum (FWHM) of Rocking curves for the films, their band gaps, and conductivities of the STO-based heterointerfaces at room temperature:

	γ-Al_2O_3	$NiAl_2O_4$	$CoAl_2O_4$	$FeAl_2O_4$
Bulk Lattice Parameter	7.911[35]	8.05[36,37]	8.10[28,38]	8.16[28,38]
Mismatch with STO Substrate (%)	1.3	3.1	3.7	4.5
FWHM of Film (deg.)	0.214	0.089	0.086	0.087
Film Lattice Parameter	8.02	8.03	8.08	8.16
Band Gap (eV)	8.7[17,39]	3.4[40]	3.6[40]	1.78[24]
Room Temperature R_s(Ω/□)	278	57.8	138	$> 10^8$

Figure captions:

FIG. 1 (a) A schematic sketch of the spinel/perovskite (MAl$_2$O$_4$/STO) oxide heterostructure (M = Fe, Co, Ni). Lattice structures of the spinel and perovskite are shown below. The box represents one unit cell, the lattice parameter of MAl$_2$O$_4$ is about twice that of STO. (b) X-ray diffraction (XRD) θ - 2θ scan of the γ-Al$_2$O$_3$, NiAl$_2$O$_4$, CoAl$_2$O$_4$, and FeAl$_2$O$_4$ films grown on TiO$_2$-terminated STO substrates. The inset shows the XRD θ-2θ scan around the STO (002) reflection. (c) Omega Rocking curves of the epitaxial films in spinel/perovskite heterostructures.

FIG. 2 (a) Temperature-dependent sheet resistances (R_s) of q-2DEGs in γ-Al$_2$O$_3$/STO, NiAl$_2$O$_4$/STO and CoAl$_2$O$_4$/STO heterostructures. (b) - (d) Magnetic dependence of Hall resistances (R_{xy}) in the three heterostructures at different temperatures, respectively. (e) Example for the determination of normal Hall effect (NHE) and anomalous Hall effect (AHE) from the total Hall effect for NiAl$_2$O$_4$/STO at 2K. Measured and calculated results are presented as thick green and thin black lines, respectively. Temperature dependence of (f) sheet carrier densities, n_s, and (g) Hall mobilities, μ, in these heterostructures.

FIG. 3 (a)-(c) Anomalous Hall resistances, R_{AHE}, in γ-Al$_2$O$_3$/STO, NiAl$_2$O$_4$/STO and CoAl$_2$O$_4$/STO heterostructures as a function of magnetic field at different temperatures. (d) Anomalous Hall resistances (at B = -10 T) as a function of temperatures for these three samples. (e) Magnetization curves as a function of magnetic field (M-H) for γ-Al$_2$O$_3$ and MAl$_2$O$_4$ (M = Fe, Co, Ni) films with a thickness of 4 nm measured at 10 K. The inset is the M-H measured at 300 K.

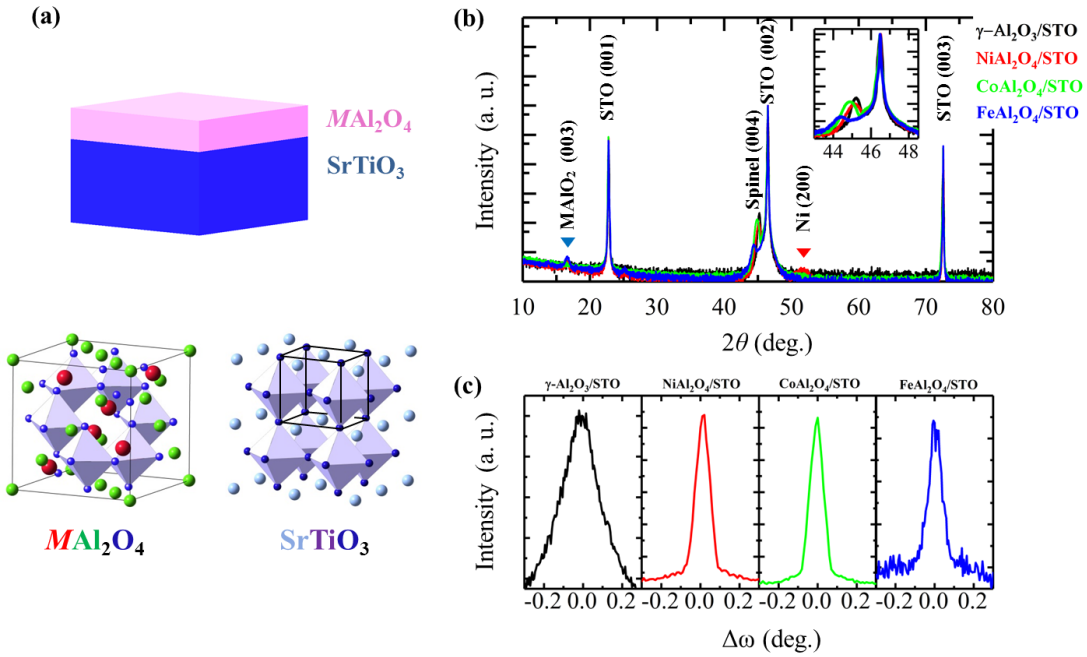
(a)
MAl_2O_4
$SrTiO_3$
MAl_2O_4
$SrTiO_3$
(b)
Intensity (a. u.)
MAlO2 (003)
STO (001)
Spinel (004)
STO (002)
Ni (200)
STO (003)
10 20 30 40 50 60 70 80
2θ (deg.)
γ–Al2O3/STO
NiAl2O4/STO
CoAl2O4/STO
FeAl2O4/STO
(c)
γ-Al2O3/STO
NiAl2O4/STO
CoAl2O4/STO
FeAl2O4/STO
Intensity (a. u.)
-0.2 0.0 0.2 -0.2 0.0 0.2 -0.2 0.0 0.2 -0.2 0.0 0.2
Δω (deg.)

FIG. 1

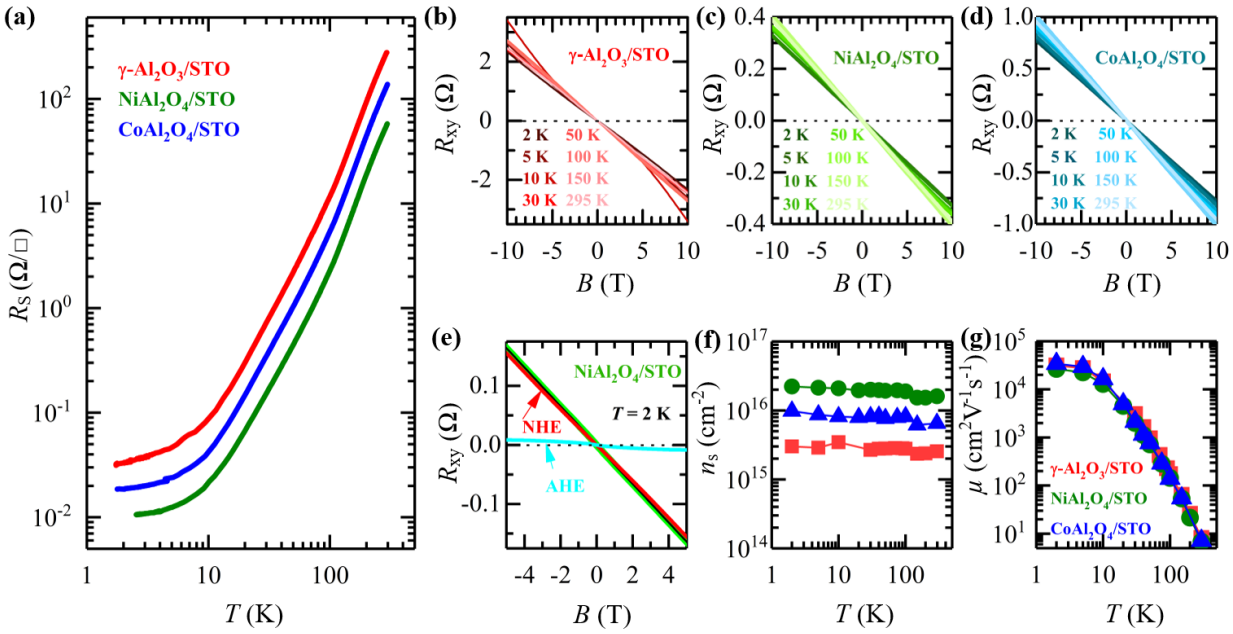
(a)
γ-Al2O3/STO
NiAl2O4/STO
CoAl2O4/STO
RS (Ω/□)
T (K)
(b)
γ-Al2O3/STO
2 K 50 K
5 K 100 K
10 K 150 K
30 K 295 K
Rxy (Ω)
B (T)
(c)
NiAl2O4/STO
2 K 50 K
5 K 100 K
10 K 150 K
30 K 295 K
Rxy (Ω)
B (T)
(d)
CoAl2O4/STO
2 K 50 K
5 K 100 K
10 K 150 K
30 K 295 K
Rxy (Ω)
B (T)
(e)
NiAl2O4/STO
T = 2 K
NHE
AHE
Rxy (Ω)
B (T)
(f)
ns (cm-2)
T (K)
(g)
γ-Al2O3/STO
NiAl2O4/STO
CoAl2O4/STO
μ (cm2V-1s-1)
T (K)

FIG.2

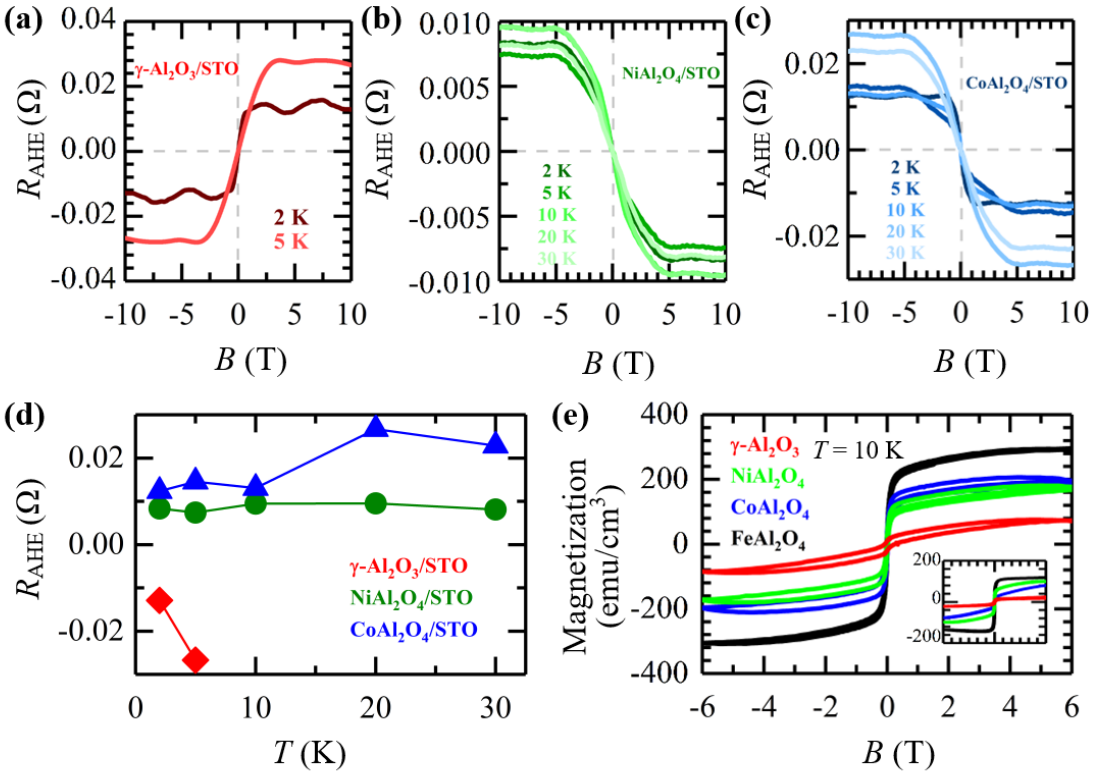
(a)
(b)
(c)
(d)
(e)
γ-Al2O3/STO
NiAl2O4/STO
CoAl2O4/STO
2 K
5 K
10 K
20 K
30 K
RAHE (Ω)
B (T)
T (K)
Magnetization (emu/cm3)
FeAl2O4
T = 10 K

FIG.3